





Disc asymmetry characterisation in JWST-observed galaxies at $1 < z < 4$

Ananya Ganapathy,¹^{*}, Michael S. Petersen,¹, Rashid Yaaqib,^{1,2}, and Carrie Filion³

¹*Institute for Astronomy, University of Edinburgh, Royal Observatory, Blackford Hill, Edinburgh EH9 3HJ, UK*

²*Department of Physics, United Arab Emirates University, Al Ain, Abu Dhabi, UAE*

³*Center for Computational Astrophysics, Flatiron Institute, New York, NY 10010*

Accepted XXX. Received YYY; in original form ZZZ

ABSTRACT

We present a novel technique using Fourier series and Laguerre polynomials to represent morphological features of disc galaxies. To demonstrate the utility of this technique, we study the evolution of asymmetry in a sample of disc galaxies drawn from the Extended Groth Strip and imaged by the JWST Cosmic Evolution Early Release Science Survey as well as archival HST observations. We measure disc asymmetry as the amplitude of the $m = 1$ Fourier harmonic for galaxies within redshift ranges of $1 < z < 4$. We show that when viewed in shorter rest frame wavelengths, disc galaxies have a higher asymmetry as the flux is dominated by star forming regions. We find generally low asymmetry at rest frame infrared wavelengths, where our metric tracks asymmetry in morphological features such as bars and spiral arms. We show that higher mass galaxies have lower asymmetry and vice versa. Higher asymmetry in lower mass galaxies comes from lower mass galaxies (typically) having higher star formation rates. We measure the relation between disc galaxy asymmetry and redshift and find no conclusive relationship between them. We demonstrate the utility of the Fourier-Laguerre technique for recovering physically informative asymmetry measurements as compared to rotational asymmetry measurements. We also release the software pipeline and quantitative analysis for each galaxy.

Key words: galaxies: star formation – galaxies: structure – galaxies: kinematics and dynamics

1 INTRODUCTION

Since the first ‘spiral nebulae’ galaxies were discovered in the 17th century, much research has been dedicated to understanding their morphology and evolution. Morphological classification systems like the Hubble Sequence (Hubble 1926) have stood the test of time as a straightforward proxy to describe galaxy evolution (Buta 2011; Buta et al. 2015). Our understanding of such classifications systems have greatly improved due to the rapid advancement of technology. The deep sky surveys by Hubble Space Telescope (HST) were revolutionary as they provided an opportunity to peer into realms never observed before (Buta 2011). However, high redshift galaxies in these surveys often cannot be resolved to the level required for detailed classification and appear to have an irregular or peculiar shape leading to a ‘classification crisis’ (van den Bergh et al. 1996; Conselice 2003). Furthermore, owing to the filters available, HST can only investigate galactic structures in the optical wavelength out until $z \approx 2.8$ beyond which only the UV rest frame wavelength can be probed (Ferreira et al. 2022; Jacobs et al. 2023). These shorter wavelengths are dominated by young forming stars (Bruzual & Charlot 2003; Jacobs et al. 2023), which can bias morphological classification.

With the commissioning of the James Webb Space Telescope (JWST) a new era in astronomy dawned. Since becoming operational, JWST has provided an opportunity to reconsider our understanding of galaxy evolution and the physical processes that govern it by lever-

aging its higher angular resolution and longer wavelength imaging capabilities (Ferreira et al. 2022). The advent of novel technology like JWST has also led to an increase in the amount of data at high redshift allowing astronomers to better classify galaxies in the early Universe. While the traditional methods like visual classification by individual science teams (e.g. Ferreira et al. 2023; Kartaltepe et al. 2023; Jacobs et al. 2023) still prevail, newer projects like Galaxy Zoo have emerged that rely on the public to classify images from datasets like the Sloan Digital Sky Survey (SDSS; Lintott et al. 2011; Smith et al. 2024). To further improve efficiency, artificial intelligence and machine learning models are also being trained on the classifications made through different citizen science projects (e.g. Gordon et al. 2024).

This paper, inspired by the work characterising detailed structure in simulations (Weinberg & Petersen 2021; Johnson et al. 2023), presents a novel classification system using a combination of Fourier and Laguerre polynomials. The combination is an effective modelling framework as they compresses large pixel datasets to a few physically meaningful coefficients. The coefficients are a description of a galactic surface brightness distribution. While visual classification becomes more ambiguous when peering into higher redshifts due to decreasing resolution, the Fourier-Laguerre method performs efficiently and reproducibly as it relies directly on quantifiable pixel information. This method can be considered as a form of unsupervised learning since it does not require prior training data (Johnson et al. 2023).

Several studies have already looked into using Fourier series to

* E-mail: a.ganapathy@sms.ed.ac.uk

describe morphological features such as bars, spiral arms and asymmetry (e.g. Reichard et al. 2009; Ghosh & Di Matteo 2024). Our model goes a step further by including Laguerre polynomials to represent the exponential surface mass density profile of disc galaxies. Early-Universe disc galaxies are crucial to characterise as they provide the key to understanding the dynamical state of the early Universe. While at high redshift the hierarchical construction of galaxies could destroy the fragile discs, observations suggests that many discs exist in the early Universe (Robertson et al. 2023). To improve our understanding of disc structures, the focus of this paper is the evolution of disc asymmetry.

In the past few decades, observational studies suggest that disc asymmetry (measured using $m = 1$ Fourier mode) show a positive correlation with starburst occurrences (e.g. Zaritsky & Rix 1997). Using a similar method, Reichard et al. (2009) also found a strong relation between asymmetry in disc galaxies and the youth of the stellar population present in SDSS galaxies. Following this, Zaritsky et al. (2013) measured the $m = 1$ related lopsidedness in a local volume-complete sample from the Spitzer Survey of Stellar Structure in Galaxies (S⁴G) survey, and concluded that the presence of structure in the dark matter halo could be sufficient to induce observed asymmetries. More recently, Yesuf et al. (2021) found that disc asymmetries correlated with higher specific star formation rate at a given stellar mass. In this work, we build on these earlier analyses and introduce a novel Fourier-Laguerre expansion framework for image analysis across multiple bands.

The paper is structured as follows. Section 2 provides context for our model and explains the working of our pipeline. In Section 3 we detail the datasets and databases referred to when identifying disc galaxies to expand through the pipeline. Section 4 presents the main results of the paper, focusing on characterizing the asymmetry of disc galaxies. Section 5 includes related discussions. The paper concludes with a synopsis of our main results and future work.

2 METHODOLOGY

We introduce a new pipeline for Fourier-Laguerre EXpansions: *FLEX*. Compared to traditional morphological classifications, *FLEX* retains more galaxy morphology information. We use *FLEX* to measure the asymmetry of galaxies by calculating the Fourier-Laguerre coefficients that best represent a given galaxy. In this section we briefly describe the technique. Further details are located in Appendices: we explain the user experience in Appendix A. The mathematical details and related uncertainties of the Fourier-Laguerre expansions are presented in Appendix B. Our treatment of centring and scale length optimisation is described in Appendix C.

Fourier series are the natural basis expansion for describing azimuthal symmetry present in galactic structure. The azimuthal structure of discs exhibits low order multiplicity (denoted m), such that Fourier expansions converge quickly (i.e. with fewer than ten harmonics). Previous studies ranging from early automated classification systems (e.g. Odewahn et al. 2002) to more recent efforts (e.g. Ghosh & Di Matteo 2024) have mainly focused on a Fourier approach in successive radial annuli to describe galaxy structure and characterise morphological features in disc galaxies such as bars and spirals. In *FLEX*, the user can choose an m_{\max} for the Fourier expansion order, setting the maximum multiplicity to be analysed. We choose $m_{\max} = 1$ in this paper, as explained below, and defer additional multiplicity investigations to future works (cf. Section 5.4).

In the radial dimension, disc galaxies largely follow an exponential surface brightness profile (Freeman 1970), with many also featuring a

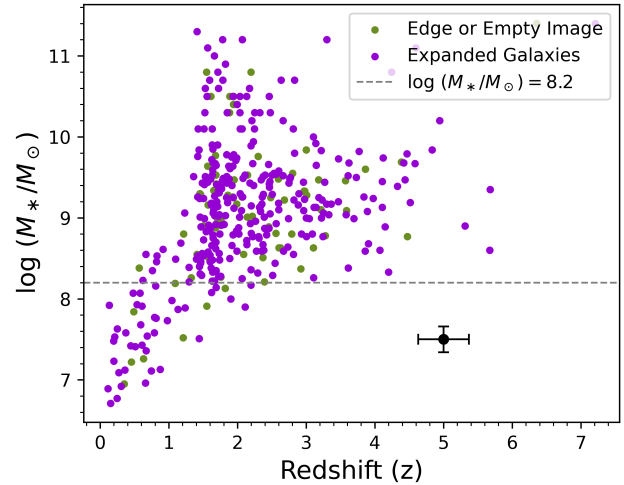


Figure 1. Distribution of 387 classified disc galaxies redshift values against their respective stellar mass as reported in *CANDELS* (Stefanon et al. 2017). The green points correspond to those that have been discarded either due to empty image arrays or being situated at the edge of the FITS image. The remaining violet data points correspond to the 271 successfully expanded galaxies. All galaxies lying over the threshold of $M = 10^{8.2}M_{\odot}$ are treated as the primary sample (Refer to Section 4). The black symbol in the lower right corner indicates the median uncertainty in redshift and stellar mass determinations for the primary sample.

super-exponential compact bulge in parametric decompositions (e.g. Díaz-García et al. 2016). Our expansion technique uses Laguerre polynomials as the radial basis functions. The exponential weighting function of Laguerre polynomials closely approximates the expected exponential profile of a typical disc galaxy, making Laguerre polynomials the ideal basis functions for expanding disc galaxies (refer to Appendix B for more detail). In *FLEX*, the user chooses a maximum Laguerre polynomial order, n_{\max} . Higher values of n_{\max} result in finer structure resolution; however, the coefficients become increasingly uncertain owing to the spatial resolution of images. We return to this point when discussing uncertainties in Appendix B.

By combining Fourier and Laguerre functions to make a two-dimensional basis, we can efficiently model the surface brightness distribution of discs in fewer terms than a corresponding Fourier-annulus expansion, with only physically motivated assumptions. The combination of polynomials enables compression of large pixel datasets to a few *physically meaningful* Fourier-Laguerre coefficients that can be used to study features like asymmetries, bars, spiral arms, and rings. We restrict our analysis in this work to asymmetries, which are the $m = 1$ set of coefficients. Furthermore, these coefficients are also unaffected by the inclination of the galaxy. As shown by several past studies (e.g. Reichard et al. 2009; Amvrosiadis et al. 2024) $m = 1$ has widely been used to track the asymmetry of a galaxy’s surface density. We further distil the radial information in the coefficients into a single metric measuring the strength of asymmetry in a galaxy, A_1 (see Appendix B for details). The A_1 metric quantifies the asymmetry of a galaxy’s light distribution.

3 DATA

For this paper, we expand disc galaxies that lie in the Extended Groth Strip (*EGS*). These galaxies were imaged by the JWST Cosmic

Evolution Early Release Science Survey (*CEERS*; Finkelstein et al. 2022) NIRCam Fields 1 - 3 and 6. We use the data reductions from the *CEERS* team (Finkelstein et al. 2022) as well as the re-reductions of the Cosmic Assembly Near-IR Deep Extragalactic Legacy Survey (*CANDELS*) HST imaging (Grogin et al. 2011; Koekemoer et al. 2011) of the same fields. Each galaxy was expanded in F444W, F410M, F356W, F277W, F200W, F115W NIRCam JWST filters. These were then complemented with HST Wide Field Camera 3 (WFC3) filters F125W and F160W and HST Advanced Camera for Survey (ACS) F606W and F814W. This gives a total of ten filters per galaxy in our sample. In the re-reduction from the *CEERS* team, all images are aligned and matched in pixel scale. *CEERS* imaging these *EGS* galaxies is complemented heavily by the extensive auxiliary data in *CANDELS*.

We use previously (visually) classified disc galaxies from the Ferreira et al. (2023) database in this work¹. These were selected by identifying galaxy IDs labelled ‘disc’ class and with a ‘True’ confidence label. In this database, any galaxy bearing a ‘True’ confidence meant that the majority class is unanimous amongst the six classifiers (Ferreira et al. 2023). From the 3956 galaxies analysed by Ferreira et al. (2023), 531 were classified as discs. Out of these 531, 144 galaxies were from the UltraDeep Survey (*UDS*) and the remaining 387 come from the *EGS*. To ensure the homogeneity of our sample, particularly in derived quantities, we focus on the 387 *EGS* galaxies. We discuss possible sample selection biases in our data sample in Appendix D. Figure 1 summarises the 387 classified *EGS* disc galaxies by plotting stellar mass² vs. best redshift³. The region between redshift 1 and 2 is densely populated while most galaxies appear to have a stellar mass ranging from $10^7 M_\odot < M_* < 10^{10} M_\odot$. To reduce sample bias, we treat galaxies with $M_* > 10^{8.2} M_\odot$ as our main sample for interpreting trends and discuss results for lower mass galaxies throughout.

For application in this paper, *FLEX* is designed to expand galaxies within a 110 by 110 pixel (3.3×3.3 arcseconds) postage stamp cutout from the *CEERS*-reduced FITS Image in each filter, accompanied by the *CANDELS* catalogue of galaxy centres. To improve the accuracy of the expansion, all non-central galaxies within this cutout are masked⁴. This automated process begins by estimating a scale radius for the galaxy from the centre of the cutout. This is done by fitting an exponential profile to the F444W image using `scipy.optimize.curve_fit` and the *CANDELS*-provided estimate for the centre. Once the initial exponential scale radius has been determined in F444W, we define a mask radius that is six times the exponential scale radius. Outside this radius, pixels that have flux above three times the median absolute deviation of the pixel intensity in the postage stamp are turned to NaN values. This technique, called sigma clipping, is thus used to ensure no contamination from foreground or background sources. The mask is then kept fixed for

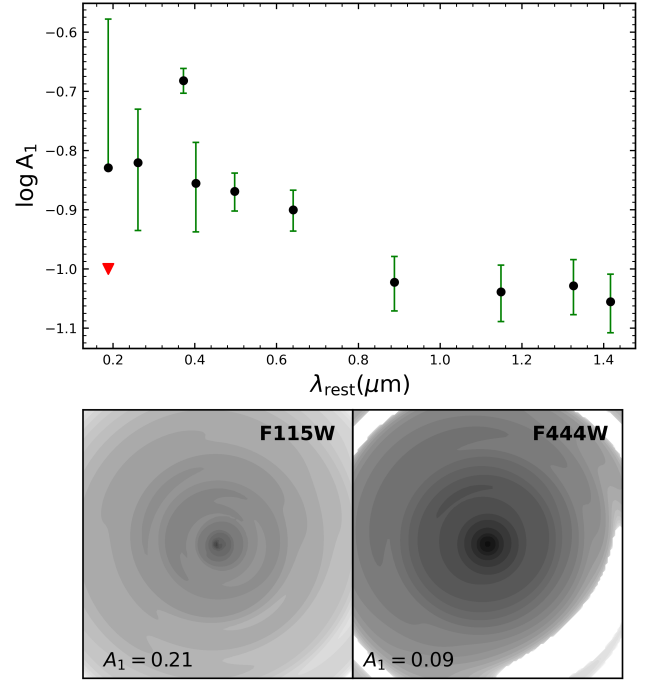


Figure 2. Top panel: Log Asymmetry of typical galaxy, EGS23205 ($\log(M_*/M_\odot) = 11.2$, $\text{SFR} = 64.83 M_\odot/\text{yr}$), as a function of rest frame wavelength (assuming $z = 2.07$). The inverted red triangle denotes that the lower limit on the lower error bar for the asymmetry measurement made in F606W extends to negative infinity (zero asymmetry). Bottom panels: (Left) Expanded surface density ($m = 1$) of EGS23205 in F115W with clumps of new stellar formation visible. (Right) Expanded surface density ($m = 1$) of EGS23205 in F444W filter, where the galaxy has a lower asymmetry value.

all filters. We summarise the uncertainties related to this masking process in Appendix B. After applying the mask, we then proceed to optimise our determination of the centre of the galaxy and tune the scale length, as detailed in Appendix C. In the end, our final sample consists of 271 successfully expanded galaxies as shown by the violet points in Figure 1⁵.

4 RESULTS

Given our *FLEX*-derived asymmetry metric, we investigate the asymmetry of galaxies (1) as a function of observed wavelength, (2) as a function of redshift, and (3) as a function of galaxy mass and specific star formation rate⁶.

⁵ During data validation, 81 galaxies were discarded due to either having empty image arrays or lying within 50 pixels of the edge of the detector, reducing the available background for the expansions. These excluded galaxies are represented by the green points in Figure 1. Besides this, 11 galaxies were eliminated as at the reported *CANDELS* coordinates, a disc galaxy was not visible.

⁶ We use *EGS* Catalogue of galaxy physical properties `6a_tau` star formation rate (Stefanon et al. 2017), which is derived using an exponentially declining star formation model. Using other estimated star formation rates does not change our conclusions.

¹ The database is hosted on GitHub and can be found [here](#). Nonparametric galaxy properties are computed using the ‘Morfometryka’ code (Ferrari et al. 2015), which we use in Appendix E.

² Obtained from the compiled *EGS* catalogue of stellar masses, `M_med`, and related uncertainties, `s_med` (Stefanon et al. 2017).

³ Obtained from compiled *EGS* catalogue of redshifts `zbest` (Stefanon et al. 2017). All redshift measurements are photometric estimates; the median uncertainty is $\sigma_z = 0.37$. This is small enough so as not to appreciably change any of our conclusions. The redshift estimates are consistent with more recent estimates (Kodra et al. 2023).

⁴ For 24 galaxies there was foreground contamination due to multiple galaxies lying close to the main galaxy. These have been removed for the purpose of this paper, and they will be further explored in future work (cf. Section 5.4).

4.1 A pedagogical example

As a pedagogical demonstration of the asymmetry calculation pipeline, Figure 2 focuses at how (the log of) asymmetry depends on rest frame wavelength for EGS23205 ($z = 2.07^{+0.17}_{-0.02}$, $\log(M_*/M_\odot) = 11.2$, $\text{SFR} = 64.83M_\odot/\text{yr}$) expanded across 10 JWST and HST filters (Refer to Section 3 for filter names). This galaxy is one of the highest redshift barred disc galaxies discovered to-date (Guo et al. 2023).

The asymmetry in EGS23205 is higher at shorter wavelengths, where emission from young stars is expected to dominate⁷. The phenomenon of increasing asymmetry at shorter wavelengths is commonly observed in the multiwavelength expansions performed here (see next Section). For EGS23205, the clump-like structures present in the spiral arms at shorter wavelength (the bottom left of Figure 2) are not visible in the longer wavelength (the bottom right of Figure 2). The clumpy appearance of star formation is further enhanced when looking at higher m_{max} as shown in Figure A1. This smoother appearance in the longer wavelengths results in a lower computed asymmetry value. The A_1 value in JWST F115W ($\lambda_{\text{rest}} = 0.37\mu\text{m}$) is high owing to prominent star formation clumps resolved in the image. The same clumps are also observed in the HST F606W ($\lambda_{\text{rest}} = 0.19\mu\text{m}$) and F814W ($\lambda_{\text{rest}} = 0.26\mu\text{m}$) filters, but the low signal-to-noise in HST images creates significant uncertainty in the measurement.

4.2 Asymmetry vs. wavelength and redshift

The top panel of Figure 3 compares the (log) median asymmetry in 25 equally distributed rest frame wavelength bins for 243 galaxies expanded through *FLEX*. We assume that asymmetry in longer wavelengths (those measured in F444W filter here) is due to ‘structural asymmetry’⁸, and A_1 in this filter has been subtracted from the asymmetry measurement of other filters. This allows us to only investigate the evolution of ‘star formation asymmetry’⁹ in disc galaxies. Once the bins have been determined and equally populated, the median A_1 value and error bars are determined in each bin. Here, the error bars represent the 1σ range of values and not the uncertainty on the mean. The strong inverse relationship suggests that the asymmetry of galaxies appears higher at shorter wavelengths. This is analogous to Figure 2 which confirms that at shorter wavelengths the determined asymmetry metric is probing new clumpy stellar formation. The longer wavelengths (last bin) in Figure 3 is dominated by low stellar mass galaxies located at low redshifts as seen in Figure 1. Hence, Figure 3 quantifies the change in median asymmetry for the last bin when considering different mass cuts. Given the practicalities of the mass sample we have, galaxies with a stellar mass $< 10^{8.2}M_\odot$ were excluded (grey points in Figure 3).

The bottom panel of Figure 3 investigates the evolution of median asymmetry in 8 equally distributed redshift bins. This has been recorded in the UV rest frame region ($0.2 < \lambda_{\text{rest}} < 0.4\mu\text{m}$) as star formation is expected to dominate the emission. A similar mass cut ($> 10^{8.2}M_\odot$) has also been applied to the sample in the bottom panel of Figure 3. The lack of observed trend suggests that the asymmetry of disc galaxies does not evolve with increasing redshift in the

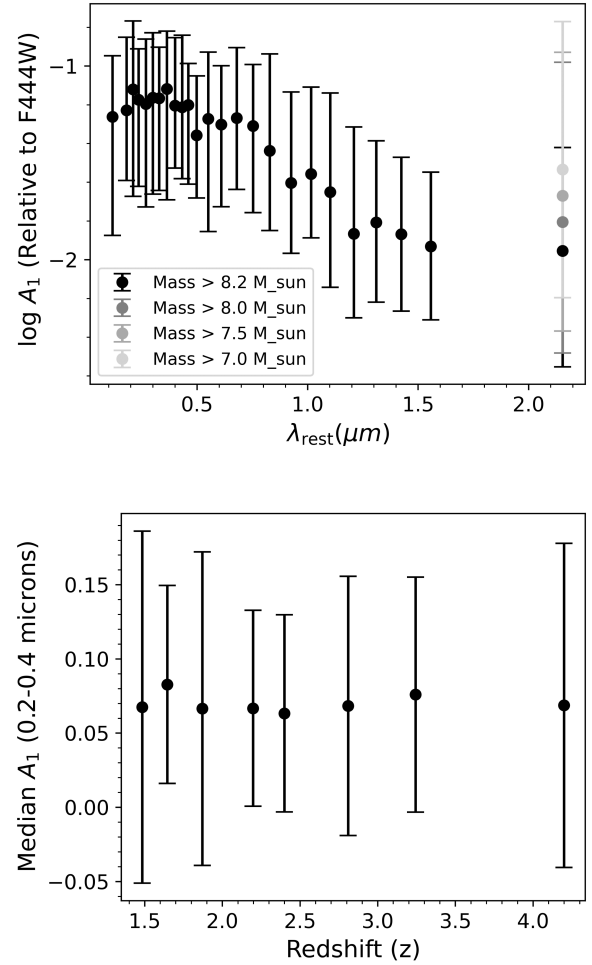


Figure 3. (Top) Log asymmetry of 243 galaxies equally distributed in 25 rest frame wavelength bins for galaxies with stellar mass $> 10^{8.2}M_\odot$. The inverse relation suggests that asymmetry appears to be higher in bluer filters where stellar formation is visible. (Bottom) Median asymmetry of 243 galaxies (stellar mass $> 10^{8.2}M_\odot$) in 8 equally distributed redshift bins. Measured in the UV rest frame region ($0.2 < \lambda_{\text{rest}} < 0.4\mu\text{m}$), there appears to be no relation between redshift and asymmetry. In both panels, the error bars denote the 1σ range of the observations, not the uncertainty on the mean.

CEERS sample, although larger mass-limited samples are required to confirm this trend.

4.3 Asymmetry vs stellar mass and star formation

Figure 4 shows galaxy stellar mass against $\log A_1$, uniformly measured in the F444W filter. Here, the asymmetry metric is probing structural asymmetry measured in the longer rest frame wavelengths. For our set of *CEERS* disc galaxies, we find that lower mass galaxies have higher associated structural asymmetry. This inverse relationship is stronger beyond a threshold of $10^{8.2}M_\odot$ (grey dashed line) which was the mass cut considered in Figure 3.

Relatedly, the structural asymmetry uncertainty is higher for smaller galaxies (refer to Appendix B for further explanation). Each galaxy in Figure 4 has also been coloured based on its redshift value as reported in *CANDELS* (Stefanon et al. 2017). Given this for a

⁷ However, short of $0.4\mu\text{m}$, the uncertainties increase owing to low overall flux from the galaxy, cf. Figure A1 and discussion in Appendix F.

⁸ That is, asymmetry that stems from asymmetry in the mass, rather than the light distribution; refer to Section 5.1.1 for further discussion.

⁹ That is, asymmetry owing to the light distribution, not necessarily reflected in the mass distribution. See Section 5.2 for further discussion.

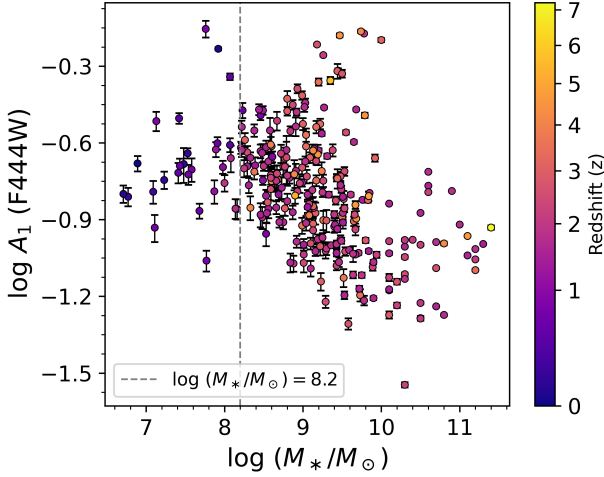


Figure 4. Stellar Mass as a function of $\log A_1$ for 271 galaxies expanded through *FLEX* in the JWST F444W filter. Each galaxy is coloured with respect to its redshift values as reported in the *CANDELS* catalogue (Stefanon et al. 2017). This plot investigates the inverse relationship between structural asymmetry and the stellar mass of a galaxy.

fixed A_1 value, higher redshift galaxies tend to have higher stellar mass as shown in Figure 1. However, studies also suggest that this could be a result of selection bias as at higher redshifts, low stellar mass galaxies become more difficult to detect (Castro-Rodríguez & López-Corredoira 2012).

Figure 5 shows the relationship between specific star formation rate (sSFR) and asymmetry as measured by our metric in the UV rest frame region ($0.2 < \lambda_{\text{rest}} < 0.4 \mu\text{m}$). Here, sSFR is defined as the ratio of SFR to stellar mass. Unlike Figure 4, the asymmetry metric here is directly investigating asymmetry in young stars as this portion of the spectrum is dominated by star formation. To improve the fit, asymmetry and sSFR values outside the 3 sigma region were clipped and a linear positive trend was fit to the trimmed data using *emcee*. The initial guesses for slope and y intercept was $[0.5, 0.5]$ and were restricted within the bounds of -10 to 10. To find the optimal parameters, 32 walkers were introduced and each simultaneously explored the parameter space for 5000 iterations. The calculated slope is $2.79^{+0.429}_{-0.415}$. Assuming that emission in the rest frame UV corresponds primarily to star formation, Figure 5 asserts that higher asymmetry corresponds to star formation as determined with respect to sSFR.

5 DISCUSSION

5.1 Asymmetry as a Dynamical Classification Tool

5.1.1 Mergers driving structural asymmetry

Mergers are widely known to affect galaxy asymmetry and are a consequence of the hierarchical formation of structure predicted by Λ -cold dark matter model (e.g. Bottrell et al. 2024).

The impact of mergers on SFR has widely been researched and observations show that mergers can trigger star formation (Pearson et al. 2019), which would appear in the shorter wavelength regime. In addition to possibly forming new stars, mergers can distort the shapes of galaxies and build their stellar masses. Stars in galaxies

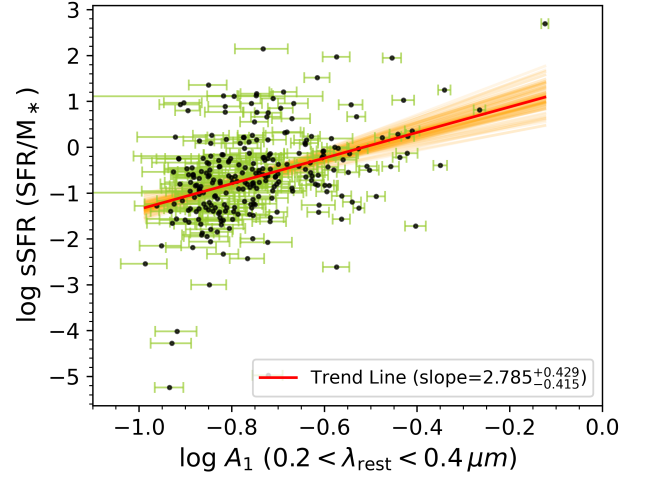


Figure 5. Disc Asymmetry of all 259 galaxies against their specific star formation rate (sSFR Stefanon et al. 2017) in log-space as measured between $0.2 < \lambda_{\text{rest}} < 0.4 \mu\text{m}$. This figure indicates that our defined asymmetry metric tracks stellar formation in the UV rest frame region.

can be traced back to either of two origins: *in situ* (stars formed from gas within the galaxy it belongs to) or *ex situ* (stars formed outside of the host galaxy in a system that has since merged, Rodríguez-Gomez et al. 2016). Hydrodynamic cosmological simulations such as the Illustris Project (Vogelsberger et al. 2014; Genel et al. 2014) have been extensively used to study the role of *in situ* and *ex situ* stars in galaxy evolution. Studies using this suite of simulations (Lackner et al. 2012; Rodríguez-Gomez et al. 2016; Pillepich et al. 2018) suggest that *ex situ* star formation prevails largely in galaxies with stellar mass $> 10^{11} M_{\odot}$. Galaxies with stellar mass $< 10^{11} M_{\odot}$ are still affected by *ex situ* star formation, however the overall fraction of *ex situ* stars is small (see Rodríguez-Gomez et al. 2016, their Figure 6). These observations are also dependent on redshift with lower redshift galaxies having higher *ex situ* star formation fractions. However, these results could be biased as with increasing redshift it is harder to resolve the effect of merger activity on disc galaxies. Referring back to Figure 1, it appears that only 7 galaxies lie above this threshold ($> 10^{11} M_{\odot}$) with most galaxies heavily populated within the range of $1 < z < 3$. In the *CEERS* disc-selected galaxies, *in situ* star formation appears dominant thus indicating that our metric is not tracking major merger activity. This conclusion is supported by examining the rotational asymmetry values from (Ferreira et al. 2023), which indicate that none of the galaxies in our sample would have been classified as mergers in the Concentration, Asymmetry, and Smoothness (CAS) system (see next subsection)¹⁰.

(Bottrell et al. 2024) measured rotational asymmetry for a sample of simulated galaxies in TNG, finding that minor (mass ratio between 0.1 and 0.25) and ‘mini’ (mass ratio between 0.01 and 0.1) mergers can drive structural asymmetry that lives on up to 3 billion years after merging. Those authors studied this by determining the offset in the Star Forming Main Sequence as it relates to the symmetry of galaxies. We call the longest wavelength measurement of the asymmetry the ‘structural asymmetry’ measurement, as even up to $z = 3$, the F444W

¹⁰ Our sample purposely selects against strong merger-driven asymmetry, as we use the sample of confidently classified discs from Ferreira et al. (2023). See discussion in Appendix D.

filter probes the infrared wavelength region, where the stellar light has a strong component from lower-mass stars that trace the long-lived stellar population. The *FLEX*-derived asymmetry measure, at first interpretation, does suggest that some galaxies may have significant asymmetry in these longer wavelengths. These galaxies are part of the lower mass sample that was excluded from the primary analysis. For all galaxies in the primary analysis, the mean asymmetry is $\langle A_1 \rangle_{F444W} = 0.15$.

5.1.2 Relationship to the CAS system

‘Asymmetry’ has, for more than two decades, meant the 180° rotational asymmetry metric from the CAS system (Conselice 2003). The utility of the rotational asymmetry measurement as a classifier was explored in detail in Conselice et al. (2000), where the metric was calibrated to a nearby sample. This work followed earlier applications to some of the then-highest redshift observations from HST (Schade et al. 1995; Abraham et al. 1996), who established algorithmic measurements as being as reliable as visual classifications at high redshift. Rotational asymmetry has often been used as a merger indicator (Conselice 2003), particularly in tandem with measures of the concentration of stellar light. When combined with galaxy colour, rotational asymmetry can distinguish spirals, ellipticals, and mergers (Conselice et al. 2000).

Our definition of an asymmetry metric is distinct from rotational asymmetry, but contains the same information. We retain many of the best qualities of rotational asymmetry measurements (e.g. low dependence on resolution) owing to the global nature of the basis functions. Additionally, we have a key advantage in our algorithmic centre-finding scheme that incorporates the technology used to define the metric, giving robust uncertainty estimates.

In Appendix E we compare our asymmetry measure directly to the CAS system. For typical low-asymmetry values in the sample, $A_1 \leq 0.3$, we find generic agreement in amplitude, but at higher asymmetry measured either via rotation or *FLEX*, we find disagreements in amplitude, suggesting that the two systems are in fact probing different properties. Tests on mock images (Appendix F) suggest that the differences owe to the effective spatial scales of asymmetry probed by the two metrics: rotational asymmetry will emphasise the asymmetries that encompass the largest pixel area, while *FLEX*-derived asymmetries will capture the strongest asymmetries relative to an unperturbed galaxy¹¹. *FLEX* has the added benefit of connecting to dynamics through simulations performed in a similar framework (e.g. Petersen et al. 2022, 2024), enhancing the interpretability of the *FLEX*-derived asymmetries. We discuss the utility of *FLEX* measurements for a standard use of rotational asymmetry – detecting mergers – in the next Section.

5.2 Asymmetry Resulting from Star Formation

Stellar evolution models show that emission at wavelengths within $0.2 < \lambda_{\text{rest}} < 0.4\mu\text{m}$ is dominated by star formation (e.g. Bruzual & Charlot 2003). In this region of Figure 2 and 3, the calculated asymmetry is relatively higher as compared to longer wavelengths. As highlighted in Section 1, asymmetry is known to track star formation which can be visually confirmed by the bottom left panel of Figure 2. Hence the observed asymptomatic behaviour in Figure 2 and 3 can

¹¹ *FLEX* can, in principle, be made to reproduce the rotational asymmetry metric by choosing a different weighting scheme for the radial coefficients that determine the asymmetry value.

be associated with the youth of stellar populations found within the galaxies. In particular, these clumps of stellar formation are present in the spiral arms as visually identified in Figure 2.

Figure 5 shows the relationship between sSFR and asymmetry as measured by our metric in the UV rest frame region ($0.2 < \lambda_{\text{rest}} < 0.4\mu\text{m}$). Assuming that emission in the rest frame UV corresponds primarily to star formation, higher asymmetry in disc galaxies in the UV likely traces star formation, and is thus correlated with higher sSFR. The Spearman correlation coefficient for this relation is 0.378 (p-value = 3.639×10^{-10}) indicating a weak positive relation between asymmetry and sSFR.

Redder filters, which probe the longer rest frame wavelengths, are advantageous when viewing larger morphological features like bars (i.e. an $m = 2$ Fourier feature; Ghosh & Di Matteo 2024) and spiral arm structure. This is because these filter sets trace the old redder stellar population, enabling the study of smooth broader galactic features. Despite not tracking young, blue stellar populations in the redder filters (e.g. the JWST F444W filter), our determined metric confirms that there exists underlying structural asymmetry in disc galaxies (Figures 2 and 3). In addition, when viewed in the near IR region, asymmetry and sSFR appear to have a negative correlation. Thus it can be assumed that our metric is recognising another asymmetry contributor that impacts the redder stars without inducing additional star formation (Refer to Section 5.3 for more information).

5.2.1 Star formation and low stellar mass: a highly asymmetric regime

Recent research indicates that for galaxies in the *CEERS* dataset, a direct relation between a galaxy’s stellar mass and sSFR can be drawn (Cole et al. 2023). A similar study using the JWST Advanced Deep Extragalactic Survey (JADES) also concluded that low mass galaxies experience more recent active star formation between $z \sim 4-9$ (Simmonds et al. 2024). At lower redshift, observations utilising the Sydney–AAO Multi-object Integral field spectrograph (*SAMI*) Galaxy Survey show that low mass galaxies have proportionately more H α gas (Bloom et al. 2017). This is a strong indicator of star formation as it traces the ionised gas of star forming H II regions (Tacchella et al. 2022). Besides this, earlier analysis utilising SDSS demonstrated that low mass galaxies are more prone to experience star bursts and young stellar formation (Kauffmann et al. 2003). Past observations can be used to support the inverse relationship seen in Figure 4. Additionally, Reichard et al. (2009) deduced that lower-mass galaxies tend to exhibit greater disc asymmetry (measured by the $m = 1$ mode) and appeared more lopsided. Building on this, Yesuf et al. (2021) introduced a data-driven framework to identify galaxy properties correlated with specific star formation rates. Asymmetry, as computed in the CAS system by Bottrell et al. (2019), was found to correlate with the position of a galaxy relative to the sSFR main sequence as a function of galaxy stellar mass.

5.3 Other Sources of Asymmetry

Beyond merger-driven asymmetry and star formation-driven asymmetry, other causes of asymmetry have been theorised: (1) Active Galactic Nuclei (AGN) activity, (2) dark matter halo (sub)structure, and (3) cosmological accretion.

AGN have been proposed as drivers of asymmetry, usually owing to their relationship with star formation. Previous observational studies have shown that radio-mode AGN feedback quenches star

formation as the energy released causes shock waves and heat which prevent clouds of gas and dust from cooling down (Fabian 2012). For galaxies in SDSS, Reichard et al. (2009) found a direct relation between asymmetry and measured power of centrally hosted AGN, suggesting that highly asymmetric galaxies may tend to host relatively more powerful AGN and hence quench star formation more. However, past research focusing on AGN within CANDELS galaxies have found that AGN do not affect galaxy asymmetry when compared to control galaxies (Villforth et al. 2014)¹².

Long-lived dark matter halo structure has been shown in simulations to create disequilibrium and asymmetries in the stellar disc, which can persist for Gyr (Grand et al. 2023; Johnson et al. 2023). Some of the structure may be induced by mergers or interactions, while other halo structure owes to natural evolutionary modes that are present in many halos (Weinberg 2023). Such asymmetries should be present at all wavelengths, as they will affect both the older stellar population as well as where star formation may be enhanced. Work connecting observed disc asymmetries to halo structure necessitates further theoretical development, but if conclusively demonstrated, disc asymmetry could provide a powerful tool to probe the dynamical state of dark matter halos as well as their substructure.

Finally, the accretion of gas along filaments can produce asymmetry. N-body simulations investigating this asymmetry suggest that cold gas accretion can form a thin, kinematically cold, lopsided disk that lives on as the disc galaxy evolves (Bournaud et al. 2005a). In this scenario, the asymmetry will show up in largely younger stars, but would also show up in any gas distribution. Future observations of either gas structure or kinematics can help determine whether gas accretion can sustain observed asymmetries in discs.

5.4 Future Prospects for *FLEX*

As discussed in Section 2, *FLEX* has currently been set up to measure disc asymmetry using the $m = 1$ mode related coefficients. However, we aim to focus future work on using higher order Fourier modes ($m = 2, 3, \dots$) to characterise morphological features such as bars and spirals after accounting for the effect of inclination and galaxy ellipticity.

Besides this, *FLEX* only expands a single galaxy within a cutout while masking background galaxies. We aim to extend its functionality to performing multiple galaxy expansions within a given pixel bound. This improvisation can be used to study inter-galactic dynamics such as mergers using the coefficients produced.

As discussed in Section 4 and Appendix C, *FLEX* produces coefficients with no direct dependence on the galaxy image resolution and redshift. Future research could leverage this feature to morphologically classify high-redshift galaxies, providing insights into the formation of the earliest disc galaxies.

Additionally, *FLEX* also lends itself to studying galaxies in the Local Group by leveraging higher-order harmonics. This is advantageous, as higher-order harmonics can help describe finer features of galaxies, such as accretion around black holes.

6 CONCLUSION

In this work, we characterise the asymmetry of 271 disc galaxies lying within the *EGS* field imaged by JWST in *CEERS* and archival HST

observations. For this work, we expand previously identified disc galaxies (Ferreira et al. 2023) within redshift ranges of $1 < z < 4$ using the *FLEX* pipeline. This novel framework uses Fourier-Laguerre polynomials to compress pixel information into coefficients that describe galaxy morphology. Compared to traditional nonparametric classification methods, *FLEX* retains information on both the exponential profile of a disc galaxy as well as physically informative deviations. In this work, we use *FLEX* to measure the asymmetry of a galaxy using the set of $m = 1$ radial coefficients. The $m = 1$ radial coefficients describe the asymmetry (lopsidedness) of galaxy light distributions. The main conclusions of our work are as follows:

(i) Asymmetry is higher at shorter rest frame wavelengths (upper panel of Figure 3). This is because in bluer filters, clumps of young stellar population dominate the emission (bottom left panel of Figure 2). Redder filters can be used to probe asymmetry of features like bars and can be used to determine the underlying structural asymmetry of disc galaxies (bottom right panel of Figure 2).

(ii) Asymmetry does not evolve with redshift in the UV rest frame region (bottom panel of Figure 3). However, a larger mass limited sample is needed to find a conclusive relation between asymmetry and redshift.

(iii) Disc galaxies with lower stellar mass are more asymmetric and vice versa in the F444W filter (Figure 4). This suggests that the structural asymmetry, determined at longer wavelengths, is inversely proportional to the stellar mass of a disc galaxy. This aligns with earlier analyses showing that lower stellar mass galaxies have higher presence of star formation rate (Cole et al. 2023; Simmonds et al. 2024). We also conclude that for a given A_1 value, higher stellar mass galaxies appear to be located at high redshifts.

(iv) The asymmetry of a disc galaxy is positively correlated with sSFR in the UV rest frame region (Figure 5). We interpret this as direct evidence that A_1 is indicative of stellar formation happening within the disc galaxy.

ACKNOWLEDGEMENTS

AG acknowledges financial support from SoPA's Physics and Astronomy Career Development Scholarship. MSP acknowledges support from a UKRI Stephen Hawking Fellowship. MSP and CF thank the EXP collaboration for feedback on an early version of this work. This work is based in part on observations made with the NASA/ESA/CSA James Webb Space Telescope and NASA/ESA Hubble Space Telescope obtained from the Space Telescope Science Institute, which is operated by the Association of Universities for Research in Astronomy, Inc., under NASA contract NAS 5–26555. These observations are associated with program(s) CANDELS. The authors of this paper utilised the following software: numpy (Harris et al. 2020), scipy (Virtanen et al. 2020), HDF5 (Fortner 1998), Matplotlib (Hunter 2007), Astropy (Astropy Collaboration et al. 2013, 2018, 2022), emcee (Foreman-Mackey et al. 2013), and lintsampler (Naik & Petersen 2024).

DATA AVAILABILITY

FITS Images for this project were taken from the *CEERS* dataset available [here](#). *CANDELS* data, used in this paper, is also publicly available [here](#). *FLEX*, created by the authors, can be accessed [here](#).

¹² A similar study focusing around $z \sim 2$ found minor asymmetries in 44% of AGN-hosting galaxies (Kocevski et al. 2012).

REFERENCES

- Abraham R. G., van den Bergh S., Glazebrook K., Ellis R. S., Santiago B. X., Surma P., Griffiths R. E., 1996, *ApJS*, **107**, 1
- Amvrosiadis A., et al., 2024, *arXiv e-prints*, p. arXiv:2407.12983
- Astropy Collaboration et al., 2013, *A&A*, **558**, A33
- Astropy Collaboration et al., 2018, *AJ*, **156**, 123
- Astropy Collaboration et al., 2022, *ApJ*, **935**, 167
- Bloom J. V., et al., 2017, *MNRAS*, **465**, 123
- Bottrell C., Simard L., Mendel J. T., Ellison S. L., 2019, *MNRAS*, **486**, 390
- Bottrell C., et al., 2024, *MNRAS*, **527**, 6506
- Bournaud F., Jog C. J., Combes F., 2005a, *A&A*, **437**, 69
- Bournaud F., Combes F., Jog C. J., Puerari I., 2005b, *A&A*, **438**, 507
- Bruzual G., Charlot S., 2003, *MNRAS*, **344**, 1000
- Buta R. J., 2011, *arXiv e-prints*, p. arXiv:1102.0550
- Buta R. J., et al., 2015, *ApJS*, **217**, 32
- Castro-Rodríguez N., López-Corredoira M., 2012, *A&A*, **537**, A31
- Cole J. W., et al., 2023, *arXiv e-prints*, p. arXiv:2312.10152
- Conselice C. J., 2003, *ApJS*, **147**, 1
- Conselice C. J., Bershadsky M. A., Jangren A., 2000, *ApJ*, **529**, 886
- Díaz-García S., Salo H., Laurikainen E., 2016, *A&A*, **596**, A84
- Fabian A. C., 2012, *ARA&A*, **50**, 455
- Ferrari F., de Carvalho R. R., Trevisan M., 2015, *ApJ*, **814**, 55
- Ferreira L., et al., 2022, *ApJ*, **938**, L2
- Ferreira L., et al., 2023, *ApJ*, **955**, 94
- Finkelstein S. L., et al., 2022, *ApJ*, **940**, L55
- Foreman-Mackey D., Hogg D. W., Lang D., Goodman J., 2013, *PASP*, **125**, 306
- Fortner B., 1998, Dr Dobb's J Software Tools Prof Program, **23**, 42
- Freeman K. C., 1970, *ApJ*, **160**, 811
- Genel S., et al., 2014, *MNRAS*, **445**, 175
- Ghosh S., Di Matteo P., 2024, *A&A*, **683**, A100
- Gordon A. J., Ferguson A. M. N., Mann R. G., 2024, *MNRAS*,
- Grand R. J. J., Pakmor R., Fragkoudi F., Gómez F. A., Trick W., Simpson C. M., van de Voort F., Bieri R., 2023, *MNRAS*, **524**, 801
- Grogin N. A., et al., 2011, *ApJS*, **197**, 35
- Guo Y., et al., 2023, *ApJ*, **945**, L10
- Harris C. R., et al., 2020, *Nature*, **585**, 357
- Hubble E. P., 1926, *ApJ*, **64**, 321
- Hunter J. D., 2007, *Computing in Science & Engineering*, **9**, 90
- Jacobs C., et al., 2023, *ApJ*, **948**, L13
- Johnson A. C., Petersen M. S., Johnston K. V., Weinberg M. D., 2023, *MNRAS*, **521**, 1757
- Kartalpe J. S., et al., 2023, *ApJ*, **946**, L15
- Kauffmann G., et al., 2003, *MNRAS*, **341**, 54
- Kocevski D. D., et al., 2012, *ApJ*, **744**, 148
- Kodra D., et al., 2023, *ApJ*, **942**, 36
- Koekemoer A. M., et al., 2011, *ApJS*, **197**, 36
- Lackner C. N., Cen R., Ostriker J. P., Joung M. R., 2012, *MNRAS*, **425**, 641
- Lintott C., et al., 2011, *MNRAS*, **410**, 166
- Naik A., Petersen M., 2024, *The Journal of Open Source Software*, **9**, 6906
- Odeh S. C., Cohen S. H., Windhorst R. A., Philip N. S., 2002, *ApJ*, **568**, 539
- Pearson W. J., et al., 2019, *A&A*, **631**, A51
- Petersen M. S., Weinberg M. D., Katz N., 2022, *MNRAS*, **510**, 6201
- Petersen M. S., Roule M., Fouvry J.-B., Pichon C., Tep K., 2024, *MNRAS*, **530**, 4378
- Pillepich A., et al., 2018, *MNRAS*, **473**, 4077
- Reichard T. A., Heckman T. M., Rudnick G., Brinchmann J., Kauffmann G., Wild V., 2009, *ApJ*, **691**, 1005
- Robertson B. E., et al., 2023, *ApJ*, **942**, L42
- Rodríguez-Gomez V., et al., 2016, *MNRAS*, **458**, 2371
- Schade D., Lilly S. J., Crampton D., Hammer F., Le Fevre O., Tresse L., 1995, *ApJ*, **451**, L1
- Simmonds C., et al., 2024, *MNRAS*, **527**, 6139
- Smith B. J., Watson M., Giroux M. L., Struck C., 2024, *AJ*, **168**, 12
- Stefanon M., et al., 2017, *ApJS*, **229**, 32
- Tacchella S., et al., 2022, *MNRAS*, **513**, 2904
- Villforth C., et al., 2014, *MNRAS*, **439**, 3342
- Virtanen P., et al., 2020, *Nature Methods*, **17**, 261
- Vogelsberger M., et al., 2014, *MNRAS*, **444**, 1518
- Weinberg M. D., 2023, *MNRAS*, **525**, 4962
- Weinberg M. D., Petersen M. S., 2021, *MNRAS*, **501**, 5408
- Yesuf H. M., Ho L. C., Faber S. M., 2021, *ApJ*, **923**, 205
- Zaritsky D., Rix H.-W., 1997, *ApJ*, **477**, 118
- Zaritsky D., et al., 2013, *ApJ*, **772**, 135
- van den Bergh S., Abraham R. G., Ellis R. S., Tanvir N. R., Santiago B. X., Glazebrook K. G., 1996, *AJ*, **112**, 359

APPENDIX A: *FLEX* PIPELINE FRAMEWORK

FLEX is an automated pipeline which can accept a list of user input *EGS* galaxy IDs and returns postage stamps, expansion coefficients, and asymmetry measurements. The process begins with locating the desired galaxy within the provided FITS images using reported (RA, Dec) values from the *CANDELS* catalogue (Stefanon et al. 2017). If a galaxy cannot be located, it is reported to the user and saved to a ‘unclassifiable’ log file. Once located, a 110 by 110 pixel postage stamp of the galaxy is created centred around the given (RA, Dec). To reduce interference, bright pixels outside the desired galaxy’s radius are masked using sigma clipping. Refer to Section 3 for detailed explanation about masking. A first estimate of the scale radius of the galaxy is determined using `scipy.optimize.curve_fit` to fit an exponential profile for the surface brightness profile of the galaxy. Following this estimate, we check that the galaxy image is not at the edge of the FITS file or empty. If it meets either of the conditions, the galaxy details are appended to the same ‘unclassifiable’ log file.

Once all filter image details are saved onto an HDF5 formatted file, the centre and scale length for the expansion (Appendix C) are determined. These values are then set as parameters in the Fourier-Laguerre coefficients calculations. The determined Fourier-Laguerre coefficients are saved onto the same HDF5 file as the filter images upon completion. To visualise the expanded surface density, the pipeline displays a contour map of the expanded surface density (Equation B5) alongside an amplitude chart for the filter the galaxy was expanded in.

Figure A1 shows how EGS23205 (cf. Section 4.1) appears in different JWST filters (upper row), with the corresponding *FLEX* expansion in the lower row. As shown in this figure, *FLEX* can be applied to several filters within a dataset to create a homogeneous description of galactic structure. Unlike the bottom panel of Figure 2 which is the expanded surface density for the $m = 1$ mode, Figure A1 explores the expansion with $m_{\max} = 8$ mode and radial order $n_{\max} = 24$. This is a representation of a higher order expansion of the same galaxy, EGS23205, across all ten filters provided by CEERS. The galaxy is well-reconstructed where the detection is significant (i.e. near the centre of the image), but aliasing appears in the outskirts. This aliasing is purely visual and does not affect our conclusions.

APPENDIX B: FOURIER-LAGUERRE POLYNOMIALS

FLEX represents galaxies using a Fourier-Laguerre 2D expansion, which has also been used in Weinberg & Petersen (2021); Johnson et al. (2023). We detail the expansion technique and define the A_1 asymmetry metric in this Appendix.

Disc galaxies tend to have an exponential surface brightness profile

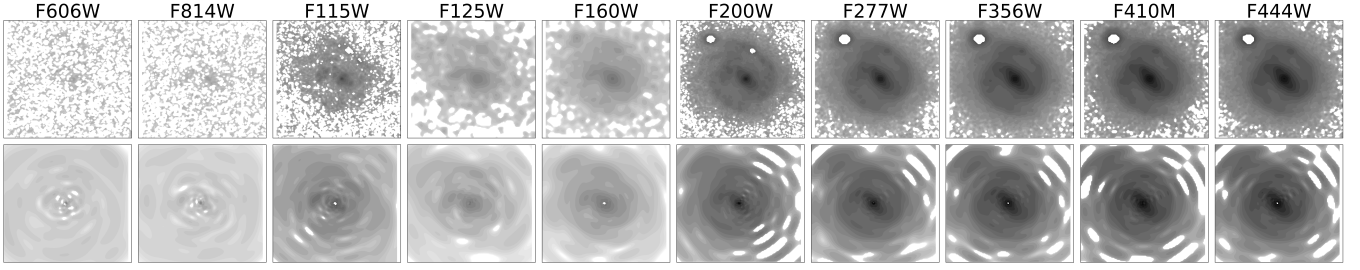


Figure A1. Surface Density of EGS23205 (Top Row) and the reconstructed surface density (Bottom Row) in JWST filters (F444W, F410M, F356W, F277W, F200W, F115W) and HST filters (F160W, F125W, F814W, F606W). The top row also demonstrates the background masking procedure (Refer Section 3 for detailed explanation) applied within a 110 by 110 pixel bound.

$$\Sigma(R) \propto \exp\left(-\frac{R}{a}\right) \quad (\text{B1})$$

where R is the 2D radius and a is the scale length of the disc.

In the radial R coordinate, Laguerre polynomials are used as the exponential weighting function matches the exponential profile of a typical disc galaxy (cf. Equation B1):

$$G_n(R) = \frac{1}{a\sqrt{n+1}} \exp\left(-\frac{R}{a}\right) L_n^1\left(\frac{2R}{a}\right). \quad (\text{B2})$$

Here, L_n^1 is the associated Laguerre polynomial of order $\alpha = 1$ and degree n , and a is the expansion scale length (chosen to be equivalent to the disc scale length). As the $n = 0$ polynomial is a constant, Equation B2 matches the expected exponential surface brightness (Equation B1). Increasing values of n adds additional ‘nodes’ to the Laguerre function, which correspond to excesses (decrements) above (below) the exponential profile.

Galaxies are often reasonably smooth in the azimuthal coordinate ϕ , with low-order multiplicity m that can be described by Fourier series. When combined, Fourier-Laguerre basis functions given by

$$f_{mn} = G_n(R) \exp(m\phi), \quad (\text{B3})$$

can accurately model the surface brightness profile of discs in two dimensions, in appropriately chosen combinations. In practice, we compute the exponential using cosine and sine, corresponding to the real and imaginary part of the expansion, respectively. Determining the weighting of each function in the expansion is straightforward, from the two-dimensional surface brightness of the galaxy,

$$\hat{c}_{mn} = \frac{1}{2\pi} \sum_x \sum_y \Sigma(R_{xy}, \phi_{xy}) G_n(R_{xy}) \cos(m\phi_{xy}) \quad (\text{B4})$$

$$\hat{s}_{mn} = \frac{1}{2\pi} \sum_x \sum_y \Sigma(R_{xy}, \phi_{xy}) G_n(R_{xy}) \sin(m\phi_{xy})$$

where the discrete summations are over individual pixels in the image, indexed by (x, y) . The reconstructed surface density at each (x, y) pixel location, $\hat{\Sigma}(R_{xy}, \phi_{xy})$, is then

$$\hat{\Sigma}(R_{xy}, \phi_{xy}) = \sum_{m=0}^{m_{\max}} \sum_{n=0}^{n_{\max}} G_n(R_{xy}) \times \left[\hat{c}_{mn} \cos(m\phi_{xy}) + \hat{s}_{mn} \sin(m\phi_{xy}) \right]. \quad (\text{B5})$$

In practice, the expansion is truncated at some maximum Fourier multiplicity m_{\max} and a maximum radial order n_{\max} , set by the quality of the data or by the user. We defer a detailed exploration of

the effect of expansion order to a future work (cf. Section 5.4). In the remainder of the work, we assume coefficients (Equation B4) are estimated from pixels, and drop the $\hat{\cdot}$ notation.

To analyse morphological features, the coefficients are quantified by computing the total amplitude A_m (for $m > 0$) in a harmonic order, normalised by the axisymmetric amplitude:

$$A_m = \sqrt{\sum_{n_{\min}}^{n_{\max}} (c_{mn}^2 + s_{mn}^2)} \bigg/ \sqrt{\sum_{n_{\min}}^{n_{\max}} (c_{0n}^2)}. \quad (\text{B6})$$

All s_{0n} terms are zero. Physically A_m quantifies the Fourier deviation from the exponential profile, in units emphasising the significance of the deviation from an axisymmetric disc. The normalisation term in the denominator is analogous to the total luminosity of the galaxy measured in native image units, here being pixels. The top panel of Figure B1 demonstrates that the expected Luminosity-Mass relationship can be retrieved through plotting the normalised axisymmetric amplitude in the JWST F444W filter, i.e. the denominator of Equation B6 against the derived stellar mass.

In the main text we restrict our analysis to the A_1 term, and will study higher harmonics in future work (Refer Section 5.4). We refer to the A_1 term as the ‘disc asymmetry’. The bottom panel of Figure B1 describes the inverse linear relationship between the uncertainty on disc asymmetry and stellar mass. For a fixed stellar mass, at higher redshift it appears that there is higher associated uncertainty in A_1 . When considering high mass galaxies, they appear more luminous and have a prominently defined galactic centre. Due to this, the model can more accurately predict the A_0 metric. Hence, the other A_m metrics such as A_1 have lower associated uncertainty as shown in Figure B1.

We treat four sources of uncertainty in the calculation of A_1 : (1) formal image uncertainty; (2) expansion truncations; (3) centre related uncertainty; (4) masking related uncertainty.

To treat formal image uncertainty (1), we create random noise realisations of the images from the reported pixel uncertainty and pass those images through the pipeline, calculating the median and standard deviation of A_1 . We also use an empirical estimate for the effect of image uncertainty on the calculation of A_0 (used in the calculation of A_1) as a function of the background relative to the galaxy peak surface brightness (see Appendix F).

To treat expansion truncation uncertainty (2), for each galaxy, we perform expansions with varying maximum Laguerre order n_{\max} and record the asymmetry values A_1 for each expansion. With increasing n_{\max} the value of A_1 converges. The n_{\max} value after which A_1 shows least variance informs the choice of the order that is required for each galaxy. In the convergence regime, the standard deviation of A_1 about the mean is recorded as the expansion truncation uncertainty. For all

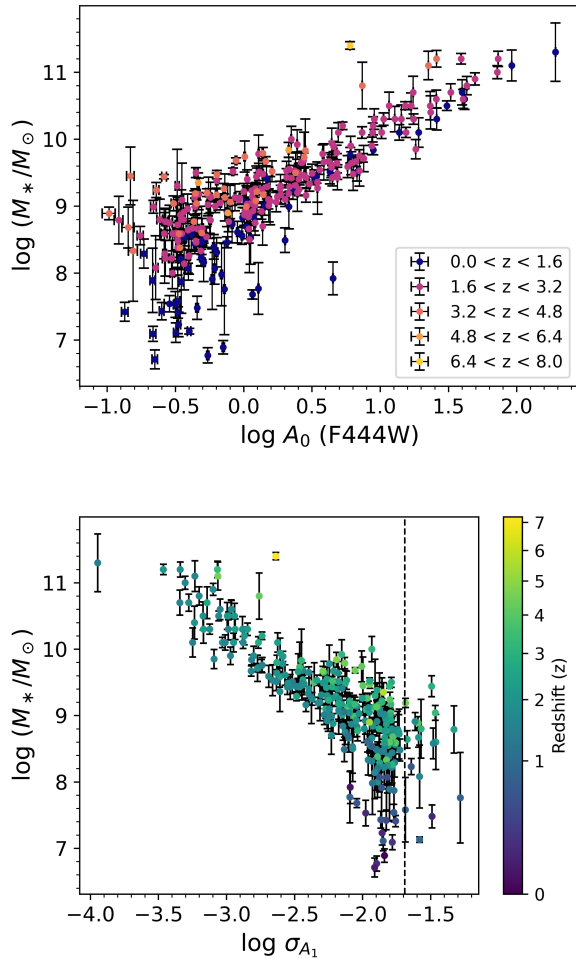


Figure B1. (Top) Scatter Plot displaying a positive linear relationship between $\log A_0$ and Stellar Mass (Stefanon et al. 2017) as measured in F444W filter. This relationship appears to be analogous to the Luminosity - Mass relationship as A_0 describes the total luminosity of the galaxy. This is because, A_0 is the lowest order term and thus carries the highest significance in the expansion. (Bottom) Scatter Plot comparing the evolution of A_1 metric uncertainty with Stellar Mass as reported in CANDELS (Stefanon et al. 2017). The points are also coloured based on their redshift values obtained from CANDELS (Stefanon et al. 2017). This figure asserts that higher mass galaxies have lesser A_1 uncertainty associated for a fixed redshift value. The vertical dashed line represents the point beyond which the uncertainty of the expansion is dominated by centre finding and truncation uncertainty.

galaxies considered here, beyond the median radial order of 12 the value of A_1 converges.

The uncertainty related to the expansion centre (3) is set by the tolerance level during the minimisation procedure described in Appendix C. The uncertainty in this case is the tolerance set of 0.01, giving a floor in the systematic uncertainty for A_1 .

The uncertainty corresponding to background galaxy masking (4) has been accounted for in two ways: error due to galaxy radius scale factor chosen and error from threshold set for sigma clipping. Tests conducted showed that decreasing the scale factor increases the asymmetry value while the increasing the threshold for sigma clipping increases the asymmetry value. Both these errors contribute

to less than 10% of a difference in values and are not a dominant source of uncertainty in the *FLEX* pipeline.

Taken together, the image related and centre finding uncertainty are the most dominant sources and are represented by the vertical dashed line in Figure B1. It can be concluded that lower mass galaxies are more dominated by these systematic errors as compared to higher mass galaxies.

APPENDIX C: CENTRING AND SCALE LENGTH OPTIMISATION

In Section 3, we use the CANDELS-reported centre to create the galaxy postage stamp. To refine our estimates for the centre and maximise the fidelity of the reconstruction, we follow a two-step procedure to (1) minimise the large-scale asymmetry, and (2) select the scale length that minimises the amplitude of the higher-order axisymmetric coefficients relative to the lowest-order axisymmetric coefficient.

To determine the centre, we define an algorithmic centre for the galaxy based on minimising the large-scale asymmetry. In practice, the centre of a galaxy is determined by minimising the a radial-term-limited dipole metric,

$$A_1 = \sqrt{\sum_{n_{\min}}^{n_{\max}} (c_{1n}^2 + s_{1n}^2)}. \quad (\text{C1})$$

Here, n_{\min} and n_{\max} are the lowest and highest radial orders considered, respectively for the expansion. When determining the centre, a smaller n_{\max} ($n_{\max} = 10$) is chosen to minimise the dipole on larger scales, while we maintain $n_{\min} = 0$, as in the main text.

Unlike fitting elliptical isophotes, this dynamic method allows the algorithm to account for non-axisymmetric features in the centre calculation. When compared to the RA and Dec values reported in the CANDELS catalogue, we find an offset with respect to the calculated centres.

To quantify the offset and determine the cause, we measure the Euclidean distance between the reported and calculated centres were determined in each filter (F444W, F410M, F356W, F277W, F200W, F115W, F814W, F606W, F125W and F160W). The results for F444W filter are shown in Figure C1. Assuming that the calculated centres (x, y) are random and independent with standard normal distributions having $\mu = 0$ and $\sigma \in (0, \infty)$, the Euclidean distance is simply the magnitude of vector (x, y) . The most appropriate distribution to quantify a random ‘offset’ is a Rayleigh distribution as depicted in the top panel of Figure C1. Meanwhile, the lower panel of Figure C1 is a scatter plot between the Euclidean distance for each galaxy in F444W filter along with its corresponding redshift value. The random scatter of data in the lower panel of Figure C1 suggests that the offset calculated is unrelated to redshift. This further proves that *FLEX* isn’t affected by redshift and can accurately track morphological features throughout the Universe. While Figure C1 only reports the results for the F444W filter, these observations are consistent across all filters.

To optimise the scale length, we minimise

$$\text{ratio} = \frac{\sqrt{\sum_{n=1}^{n_{\max}} c_{0n}^2}}{c_{00}} \quad (\text{C2})$$

where c_{00} represents the zeroth order axisymmetric (monopole) coefficient for $m, n = 0$. In physical terms, this is akin to the total pixel intensity or luminosity of the galaxy. Similarly, c_{0n} is the axisymmetric coefficient only in the radial direction as m is fixed to 0. An

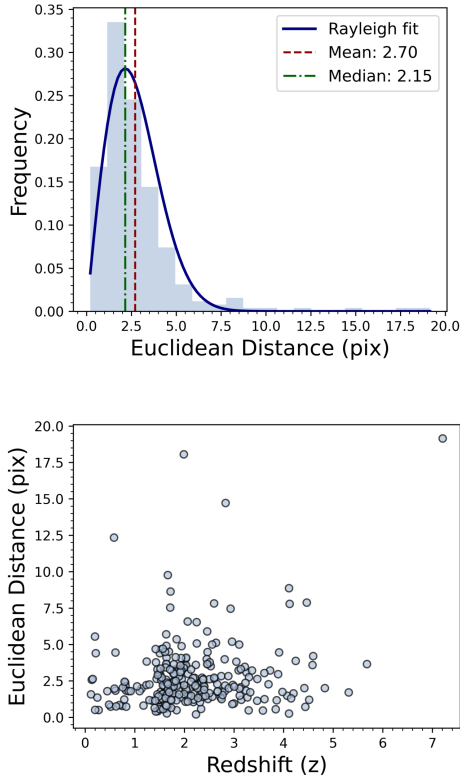


Figure C1. (Top) Rayleigh distribution of the offset in centre values from *CANDELS* catalogue (Stefanon et al. 2017) to calculated values in F444W filter. This distribution suggests that the calculated centres are random variables. (Bottom) Scatter plot comparing the centroid offset in the F444W filter with its corresponding redshift value for each galaxy. The random scatter of points suggests that our determined centre is not redshift dependent when compared to *CANDELS*-computed centres.

optimal scale length for the expansion is one that minimises Equation C2. *FLEX* is structured such that this is initially found in the F444W filter before keeping it fixed for all the other filters. This is because F444W filter has the longest effective wavelength of $4.35\mu\text{m}$, giving the best determination of the mass distribution of the galaxy.

Physically, Equation C2 measures how the luminosity of a galaxy spreads radially and can be used to determine when the light goes from being centrally concentrated to being extended radially.

APPENDIX D: SAMPLE SELECTION AND POSSIBLE BIAS

Section 3 describes the dataset used to expand disc galaxies. As we utilised only unanimously agreed upon disc galaxies in the Ferreira et al. (2023) database, it is possible that our dataset is biased towards a particular class of disc morphology. For reference, any classification bearing a ‘False’ indicator meant that at least one of the six visual classifiers in (Ferreira et al. 2023) disagreed with the majority classification. While selecting only confident morphological discs ensures consistency in classifications, the number of disc galaxies identified within the *CEERS* Image Releases is likely underestimated, and may

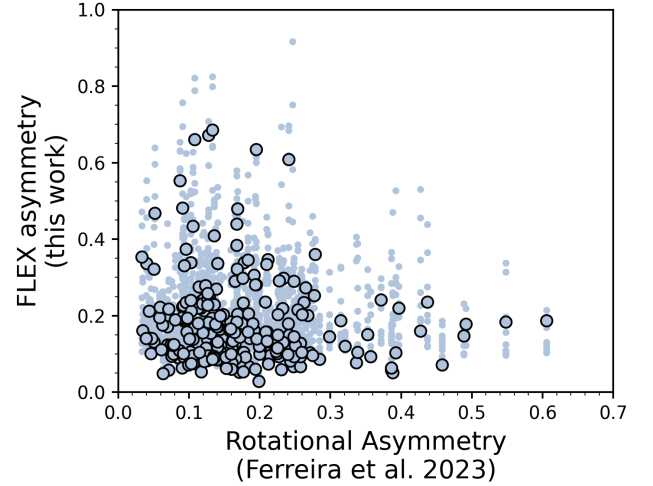


Figure E1. Comparison of rotational asymmetry (Ferreira et al. 2023) and *FLEX*-derived asymmetry. Ferreira et al. (2023) measurements are made in restframe optical bands per galaxy; for the *FLEX*-derived asymmetry we show the value in each filter, demonstrating that in no filter do we find mapping between the metrics.

be biased towards lower stellar mass galaxies with lower structural asymmetry.

On the other hand, Ferreira et al. (2023) states that disc galaxies were visually identified by looking for features such as concentrated bulges and disc envelopes alongside more prominent features such as spiral arms and bars. As the authors note, these features are harder to recognise at higher redshift and could be confused with spheroids. This potentially biases the classifications at higher redshift where image resolution is reduced, with the inclusion of spheroidal galaxies, which tend to have lower rotational asymmetry (Conselice 2003).

Similarly as the inclination of a galaxy increases, a disc galaxy can appear barred and features such as spiral arms are not visible when edge on. This could lead to ambiguity when trying to classify between galaxy morphology types and lead to a biased dataset. Bournaud et al. (2005b) also notes that when a disc galaxy is not observed face on, fitting Sersic profiles is not a reliable classification method. This is because the surface density profile is no longer exponential and the range over which the light is well-fit by a Sersic profile is reduced as the bulge covers the disc. Hence, the deviation of a galaxy profile from an exponential profile can bias our initial step of background masking and coefficient determination. Furthermore, when observing disc galaxies edge on, its radial luminosity profile could be altered due to dust attenuation.

APPENDIX E: COMPARISON WITH ROTATIONAL ASYMMETRY

In Section 5.1.2, we qualitatively discuss the relationship between our defined asymmetry metric (Equation B6) and the rotational asymmetry metric discussed in detail in Conselice (2003).

Figure E1 shows a direct comparison of rotation asymmetry from Ferreira et al. (2023) and our *FLEX*-derived asymmetry. In no regime do we find obvious agreement, and we find particular disagreement at high asymmetry values in either metric. Our *FLEX*-based procedure is more similar to residual asymmetry (e.g. Bottrell et al. 2024), which

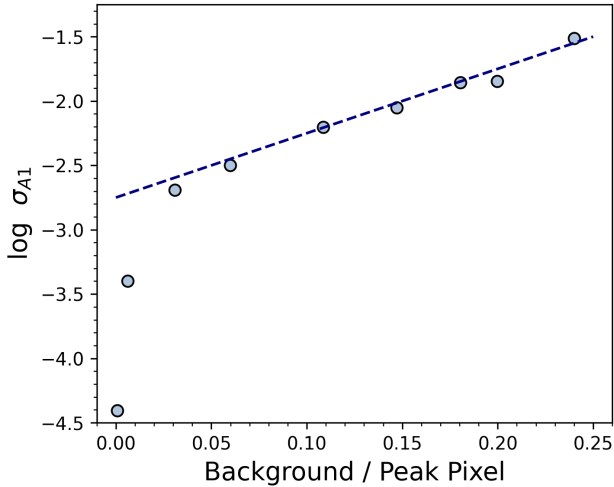


Figure F1. Empirical calibration of the effect of increasing background noise (measured as the background level divided by the peak pixel in the image) on the uncertainty estimating A_1 ($\log_{10} \sigma_{A_1}$). The uncertainty floor from centring (cf. Appendix C) is $\log_{10} \sigma_{A_1} = -2$, such that the background is only a significant source of uncertainty when $S/N \lesssim 6$. This is only true for a small handful of galaxies in our primary sample, in specific filters.

is supported by our conceptually similar results (e.g. the relationship of asymmetry with star formation).

The difference between asymmetry measures is not an issue for any interpretations advanced in this work; the result simply means that the measure of asymmetry from *FLEX* is conceptually different from rotational asymmetry. Work following similar exercises to Conselice (2003), e.g. using local galaxies as a calibration, may be a useful future study.

APPENDIX F: MOCK IMAGE MEASUREMENTS

To demonstrate the utility and fidelity of *FLEX* for measuring asymmetries, we perform two tests. First, measurement on an unperturbed galaxy to determine an uncertainty floor on A_1 from images with varying levels of observational noise, and second, an injection test, where we purposely deform a galaxy and recover the deformation.

In the first test, we realise an exponential disc of points (stars) and then ‘observe’ the stars with varying pixel resolutions and increasing noise levels (as a function of peak surface brightness of the disc). The asymmetry measurement in this case should be zero, as the galaxy is realised to be perfectly symmetric. Any deviation from zero is the result of observing the mock galaxy, both in resolution and in image uncertainty. We find that in general, the measurement uncertainty of A_1 increases with increasing ratio of the background noise to the peak pixel, without increasing bias. High background (relative to the central galaxy) can affect A_0 , which in turn will increase A_1 (which uses A_0 as a normalisation term). We use our model exponential disc to estimate the uncertainty contribution from A_0 by testing noise injection. Noise is injected into an image at varying levels with respect to the original galaxy image, and then we measure the results. The contribution of background measurement noise to A_1 uncertainty becomes significant (relative to other sources of uncertainty) at a ratio of background-to-peak pixel of 0.15, or (inverted to find) peak image $S/N \approx 6$. We use an empirically calibrated uncertainty measure,

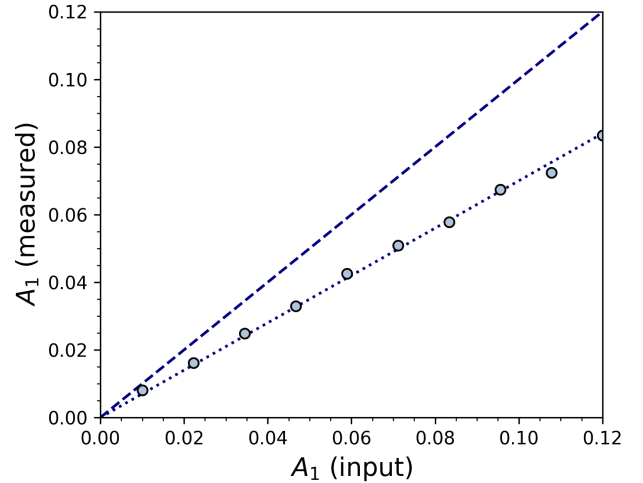


Figure F2. Recovery of asymmetry input to a model galaxy. We realise asymmetric galaxies as in the text, and measure the recovery by *FLEX*. The dashed line indicates perfect recovery; we find that we recover 70 per cent of the input asymmetry in this test (dotted line).

$\log_{10} \left(\sigma_{A_1}^{\text{background}} \right) = 5 \left(\frac{\text{background}}{\text{peak pixel}} \right) - 2.75$. This is shown in Figure F1. The effect of the background on the calculation of A_0 is not reflected in the formal image uncertainties, as the image uncertainty does not create bias in A_0 , and as such, the Monte Carlo realisations of A_1 (e.g. as described in Appendix B) do not vary strongly. This contribution to the overall uncertainty dominates the shorter wavelength points in Figure 2, where the HST images have significantly less flux overall compared to their background (cf. Figure A1).

We test the effect of pixel resolution by varying the pixels used to ‘observe’ the model exponential disc, finding that once the uncertainty from the background level has been accounted for, the effect of pixel resolution is subdominant to other uncertainty terms, contributing at approximately the 0.05 per cent level.

In the second test, we again use the mock exponential galaxy. We first compute the expansion values and zero all but the contribution from the lowest-order term. We then set a value of one $m = 1$ coefficient, and use this to create an asymmetric galaxy image by drawing 10^6 random ‘stars’ from the specified surface density¹³ and observing them by pixelating the samples.

We find that the recovery of the input A_1 value follows a monotonic trend, which confirms the ability of *FLEX* to recover asymmetry trends. The recovery is at a consistently lower value than the input, which we attribute to imperfect sampling of the mock galaxy reconstruction. We empirically estimate to be 30 per cent from a linear fit to the data. We do not expect this significant of a bias in the *FLEX*-derived measurements for real galaxies, and emphasise that the trend is the important quality to recover. In Figure F2, we show the empirical recovery of A_1 as a function of input A_1 , demonstrating our findings.

This paper has been typeset from a $\text{\TeX}/\text{\LaTeX}$ file prepared by the author.

¹³ Using *lintsampler* (Naik & Petersen 2024).